https://doi.org/10.5194/egusphere-2026-6551
Preprint. Discussion started: 6 November 2026
© Author(s) 2026. CC BY 4.0 License.

Contrasting Turbulent Transport of $PM_{2.5}$ and Conventional Scalars during Pollution Episodes over the North China Plain

Wenyao Jiang[1,2], Yan Ren[1,2], Hongsheng Zhang[3], Jiening Liang[2], Xianjie Cao[2], Pengfei Tian[2], Lei Zhang[1,2], Jianping Huang[1]

[1]Collaborative Innovation Center for Western Ecological Safety, Lanzhou University, Lanzhou 730000, China
[2]Key Laboratory for Semi-Arid Climate Change of the Ministry of Education, College of Atmospheric Sciences, Lanzhou University, Lanzhou 730000, China
[3]Department of Atmospheric and Oceanic Sciences, School of Physics, Peking University, Beijing 100081, China

Correspondence to: Yan Ren (ry@lzu.edu.cn)

Abstract.

Understanding turbulent transport similarities between $PM_{2.5}$ and conventional scalars and the origins of their differences is essential for assessing particulate turbulent diffusion relationships. Using intensive wintertime observations in Dezhou, North China Plain, we developed a retrieval method that selects visibility–$PM_{2.5}$ relationships for individual pollution episodes. This improves applicability across episodes compared with a single fixed relationship and yields $PM_{2.5}$ mass concentration fluctuations and turbulent fluxes. Estimates were more sensitive to relationship selection under low visibility, highlighting the importance of accounting for episode differences. Comparisons with CO_2, water vapour, and temperature revealed similar variance-scaling exponents but markedly lower normalized vertical transport efficiency for $PM_{2.5}$. Under unstable stratification, normalized standard deviations of all four scalars approximately followed $(-z/L)^{-1/3}$ scaling. $PM_{2.5}$ had the largest fitted coefficient, indicating stronger fluctuations relative to its flux scale, and weaker correlations with vertical velocity under both unstable and stable conditions. Strong instantaneous $PM_{2.5}$ transport events were less directionally organized than those of conventional scalars, with upward and downward contributions cancelling each other. Flux contributions at different frequencies also showed stronger cancellation between opposing directions. These event and frequency characteristics jointly explain the lower normalized vertical transport efficiency of $PM_{2.5}$. Our findings demonstrate that similar variance-scaling exponents can coexist with different transport efficiencies, extending scalar comparisons to net flux formation. They provide observational evidence for assessing shared turbulent diffusion relationships for particulate matter and conventional scalars in air quality models and improving $PM_{2.5}$ turbulent diffusion parameterizations.

1 Introduction

Fine particulate matter with aerodynamic diameters ≤ 2.5 μm ($PM_{2.5}$) is a major pollutant affecting air quality and human health. Near-surface variations in $PM_{2.5}$ concentration are influenced by emissions and regional transport and are also closely linked to turbulent transport within the boundary layer (Burnett et al., 2018; Li et al., 2017; Jin et al., 2020; Miao et al., 2018).

https://doi.org/10.5194/egusphere-2026-6551
Preprint. Discussion started: 6 November 2026
© Author(s) 2026. CC BY 4.0 License.

In contrast to mean concentration, the turbulent mass flux of $PM_{2.5}$ directly represents the net vertical exchange driven by turbulence at the measurement height (Ren et al., 2020). Turbulent diffusion of $PM_{2.5}$ is important for accurate prediction of haze pollution. In simulations of severe haze episodes over the Beijing–Tianjin–Hebei region, Wang et al. (2018) found that modeled $PM_{2.5}$ concentrations approached the observed peaks only when the turbulent diffusion coefficient was reduced. Therefore, examining $PM_{2.5}$ mass fluxes and turbulent transport helps clarify pollutant accumulation and vertical redistribution in the surface layer. It also provides observational evidence for representing particle turbulent diffusion in models (Ren et al., 2021; Jia and Zhang, 2021).

The eddy covariance method derives turbulent fluxes by simultaneously measuring the high-frequency fluctuations in both vertical velocity and a scalar and then calculating their covariance (Hicks and Baldocchi, 2020). Three-dimensional sonic anemometers and fast-response infrared gas analyzers typically measure three-dimensional wind velocity, sonic temperature, CO_2, and water vapour synchronously at 10 Hz or higher, providing the high-frequency data needed to characterize their turbulent fluctuations (Baldocchi et al., 2001; Hicks and Baldocchi, 2020; Baldocchi, 2020). Particle number fluxes can be measured using fast-response particle instruments. However, because particle number and mass concentrations weight particle size differently, number fluxes cannot directly represent $PM_{2.5}$ mass fluxes (Mårtensson et al., 2006; Ripamonti et al., 2013; Pryor et al., 2017; de Jesus et al., 2019). Several indirect estimation methods have been developed in previous studies. Ren et al. (2020) developed a visibility-based method to retrieve fine-particle mass concentration fluctuations and combined it with the eddy covariance method to estimate turbulent fluxes. Yuan et al. (2016, 2024) proposed using a large-aperture microwave scintillometer to estimate fine-particle concentration line fluxes at the hundred-metre scale. Comparison with the visibility-based retrieval method showed good agreement between the two approaches. Ren et al. (2021) compared the turbulent diffusivities of $PM_{2.5}$, momentum, and heat at three sites over the North China Plain and identified limitations in directly using heat diffusivity as a substitute for $PM_{2.5}$ diffusivity. Using the fine-particle turbulent diffusion parameterization of Ren et al. (2020), Jia et al. (2021) improved WRF-Chem simulations of wintertime $PM_{2.5}$ concentrations over eastern China.

Although visibility-based retrieval methods have been widely applied in observational and modeling studies of haze pollution, they still have some limitations. Ren et al. (2020) used a power-law relationship between visibility and $PM_{2.5}$ as an empirical model to estimate $PM_{2.5}$ mass concentration fluctuations. However, the visibility–$PM_{2.5}$ relationship can vary with pollution stage, emission sources, and air-mass conditions (Wang et al., 2006; Cheng et al., 2017). Empirical relationships obtained across different regions, seasons, and pollution conditions can take various forms, such as exponential, power-law, and logarithmic relationships. Accordingly, whether a single visibility–$PM_{2.5}$ relationship is applicable across different pollution episodes remains to be evaluated.

The near-surface turbulent transport of conventional scalars such as temperature, water vapour, and CO_2 is supported by a well-developed theoretical framework and extensive observational evidence (Moriwaki and Kanda, 2006; Guo et al., 2009). Many air-quality model parameterizations assume that $PM_{2.5}$ and temperature share the same turbulent diffusion characteristics (Jia et al., 2021; Ren et al., 2021). Comparing $PM_{2.5}$ with conventional scalars helps test the similarity of their turbulent transport and assess whether conventional scalar transport relationships apply to $PM_{2.5}$ vertical exchange. Assessing differences

https://doi.org/10.5194/egusphere-2026-6551
Preprint. Discussion started: 6 November 2026
© Author(s) 2026. CC BY 4.0 License.

in turbulent transport between $PM_{2.5}$ and conventional scalars requires consideration of both fluctuation amplitude and its covariation with vertical velocity. The flux-variance relationship describes how scalar fluctuation amplitude varies with atmospheric stability (Guo et al., 2009). The correlation coefficient quantifies the overall relationship between vertical velocity and scalar fluctuations. Quadrant and spectral analyses reveal the contributions of instantaneous events and different frequencies to the net flux, respectively (Moriwaki and Kanda, 2006; Li and Bou-Zeid, 2011). By comparing the cospectra of aerosol particles with those of heat and water vapour, Vong et al. (2010) found that differences in turbulent transport between particles and conventional scalars were scale dependent. Dupont et al. (2019) compared the quadrant contributions and timescale characteristics of dust, heat, and momentum, and identified the intermittency of dust emissions as a key factor in their different responses to turbulent structures. Previous studies have shown that particle transport differs from that of heat, water vapour, and momentum in terms of dominant transport events and characteristic scales, although most existing work has focused on particle number concentration. For $PM_{2.5}$ mass concentration, however, the similarities and differences in near-surface turbulent transport relative to conventional scalars such as CO_2, water vapour, and temperature remain poorly understood.

Overall, understanding the similarities and differences in turbulent transport between $PM_{2.5}$ and conventional scalars is important for evaluating the applicability of turbulent diffusion relationships to particulate matter. Accurate determination of the visibility–$PM_{2.5}$ relationship is essential for retrieving high-frequency $PM_{2.5}$ concentration fluctuations. It further affects the accuracy of mass-flux estimates and the analysis of turbulent transport characteristics. The North China Plain, where $PM_{2.5}$ pollution frequently occurs in winter, is a representative region for studying particle turbulent transport under severe pollution conditions. Based on comprehensive wintertime observations of the atmospheric boundary layer and atmospheric environment in Dezhou, North China Plain, this study addresses the following questions: How does the visibility–$PM_{2.5}$ relationship affect estimates of $PM_{2.5}$ concentration fluctuations and mass fluxes? What are the similarities and differences in turbulent transport between $PM_{2.5}$ and conventional scalars? Sect. 2 describes the observations and analysis methods. Sect. 3 examines the visibility–$PM_{2.5}$ relationship and differences in turbulent transport between $PM_{2.5}$ and conventional scalars. Sect. 4 presents the main conclusions.

2 Materials and methods

2.1 Field campaign

This study used data from an intensive atmospheric boundary layer and environmental campaign conducted in Dezhou, North China Plain (37.15° N, 116.47° E), from December 2018 to January 2019 (Fig. 1). The observations included three-dimensional wind velocity, temperature, water vapour, and CO_2 measured by an IRGASON (Campbell Scientific Inc., USA). $PM_{2.5}$ mass concentration and high-frequency visibility were measured using an E-sampler (Met One Instruments Inc., USA) and a modified CS120A (Campbell Scientific Inc., USA), respectively. The measurements were made at 2.8 m above ground level.

https://doi.org/10.5194/egusphere-2026-6551
Preprint. Discussion started: 6 November 2026
© Author(s) 2026. CC BY 4.0 License.

A detailed description of the field experiment and data acquisition can be found in Ren et al. (2020). All observed variables were processed at 30 min intervals, including averaging and outlier removal, to obtain the corresponding mean values. A daily mean $PM_{2.5}$ concentration of 75 μg m^{-3}, the Grade II limit in China's National Ambient Air Quality Standard, was used to separate clean and polluted periods.

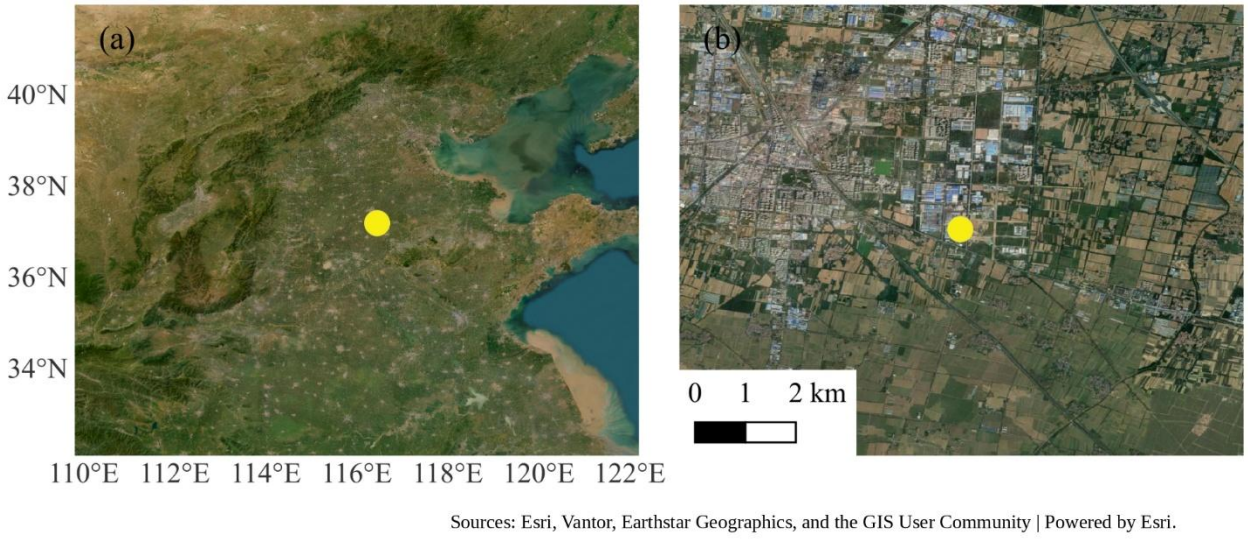


Figure 1: Location of the observation site in Dezhou and characteristics of the surrounding land surface. (a) Location of the observation site within the North China Plain and surrounding regions. (b) Satellite image showing the observation site and the surrounding local surface characteristics; the yellow marker indicates the site location.

2.2 Data preprocessing and quality control

Raw high-frequency turbulence data were preprocessed using EddyPro software (advanced mode, version 6.2.1; LI-COR Biosciences Inc., USA), with a 30 min averaging interval used for calculating turbulent statistics. The main processing steps included outlier removal, spike-noise reduction, double coordinate rotation, and mean detrending. These procedures yielded the friction velocity u_*, Monin–Obukhov length L, and turbulent fluxes of scalars such as sensible heat flux, water vapour, and CO_2. The 1 Hz high-frequency visibility data from the CS120A were also processed using spike removal and blockwise mean detrending.

$$u_* = \left[-\overline{(u'w')}^2 + -\overline{(v'w')}^2 \right]^{1/4} \quad (1)$$

$$L = -\frac{\bar{\theta} u_*^3}{\kappa g \overline{w'\theta'}} \quad (2)$$

https://doi.org/10.5194/egusphere-2026-6551
Preprint. Discussion started: 6 November 2026
© Author(s) 2026. CC BY 4.0 License.

where u', v' and w' are the longitudinal, lateral, and vertical wind velocity fluctuations (m s^{-1}), respectively; θ' is the potential temperature fluctuation (K); κ is the von Kármán constant (0.4); and g is the gravitational acceleration (9.81 m s^{-2}).

To ensure the reliability of the analysis, quality control was applied to the 30 min samples. Only samples with relative humidity (RH) below 80 % were retained. Only samples with wind directions between 60° and 300° were retained to reduce the influence of wake effects from the probes and supporting structures. Only samples with quality flags of 0 or 1 for $PM_{2.5}$, CO_2, water vapour, and sensible heat fluxes were retained, while those with a flag of 2 or missing flags were excluded. Records with obvious instrument malfunctions, prolonged data gaps, or unrealistic abrupt changes were also excluded. After quality control, the observations were classified into three stability regimes using the stability parameter $\zeta = z/L$: unstable ($\zeta < -0.05$), near-neutral ($-0.05 \le \zeta \le 0.05$), and stable ($\zeta > 0.05$).

2.3 Flux-aligned quadrant and hole analyses

To compare the organization of instantaneous transport events among scalars under different net-flux directions, we defined sign-adjusted scalar fluctuations according to the sign of the mean flux in each 30 min period:

$$s_f' = \mathrm{sgn}\left(\overline{w's'}\right)s' \tag{3}$$

where s' denotes the fluctuation in $PM_{2.5}$, CO_2, water vapour, or temperature, and s_f' denotes the sign-adjusted scalar fluctuation. After this transformation, Q1 ($w' > 0, s_a' > 0$) and Q3 ($w' < 0, s_a' < 0$) always represent instantaneous flux contributions in the same direction as the corresponding 30 min net flux, whereas Q2 and Q4 represent contributions opposite to the net-flux direction.

Based on this framework, quadrant analysis and hole analysis were used to identify instantaneous transport events of different intensities (Lu and Willmarth, 1973; Katul et al., 1997). The hole condition was defined as:

$$\left|w's_f'\right| \ge H\sigma_w\sigma_s \tag{4}$$

where H is the hole threshold, with H = 0, 1, 2 and 3. As H increases, only events with larger flux magnitudes relative to the $\sigma_w\sigma_s$ are retained.

For a given H, the absolute flux contribution from quadrant i is defined as:

$$P_i(H) = \frac{\sum_{n=1}^{N}\left|w'(n)s_{a,n}'\right| I_{i,n}M_{H,n}}{\sum_{n=1}^{N}\left|w'(n)s_{a,n}'\right| M_{H,n}} \times 100\% \tag{5}$$

where $I_{i,n}$ indicates whether the nth sample belongs to quadrant i, and $M_{H,n}$ indicates whether the sample satisfies the hole condition.

The dominant-quadrant contribution fraction is then defined as:

https://doi.org/10.5194/egusphere-2026-6551
Preprint. Discussion started: 6 November 2026
© Author(s) 2026. CC BY 4.0 License.

$$Q_{\max} = \max_{i=1,2,3,4}\left[\frac{p_i(H)}{100}\right] \tag{6}$$

Meanwhile, normalized quadrant entropy was used to quantify the dispersion of contributions among the four quadrants:

$$H_Q(H) = -\frac{\sum_{i=1}^{4} p_i(H)\, Inp_i(H)}{In4} \tag{7}$$

The H_Q ranges from 0 to 1. A value of 1 denotes equal contributions from the four quadrants, while lower values indicate greater concentration of flux contributions in fewer quadrants.

2.4 Spectral and Ogive analyses

We used frequency-premultiplied normalized variance spectra, cospectra, squared coherence spectra, and phase spectra to examine scalar fluctuations, scalar flux contributions, and scalar–vertical velocity coupling across different frequency scales. To characterize the cumulative formation of net flux from cospectral contributions, we calculated a signed Ogive function from high to low frequencies:

$$O_S(f) = \int_f^{f_N} Co_{ws}(\nu)\, d\nu \tag{8}$$

Each Ogive curve was normalized by its maximum absolute value, and a net cospectral consistency index was then defined to quantify the sign consistency of contributions across frequencies:

$$R_{net} = \frac{\left|\int_0^{f_N} Co_{ws}(f)\, df\right|}{\int_0^{f_N} \left|Co_{ws}(f)\right| df} \tag{9}$$

Where,

$$0 \le R_{net} \le 1$$

where $R_{net} = 1$ indicates that the cospectral contributions at all frequency scales have the same sign, whereas lower values indicate stronger cancellation between cospectral contributions of opposite signs.

3 Results

3.1 Overview of the pollution episodes

There were 10 pollution episodes with daily mean $PM_{2.5}$ concentrations above 75 μg m^{-3} during the observation period. Their durations are indicated by the gray shading in Fig. 2. During the pollution episodes, the mean $PM_{2.5}$ concentration was 183.92 μg m^{-3}, with a maximum of 676.05 μg m^{-3}. Visibility generally varied inversely with $PM_{2.5}$ concentration, and the mean visibility during the pollution episodes was 4.76 km. Figure 2c-f further presents the temporal variations in wind speed, air temperature, relative humidity, and stability parameter during the pollution episodes. Near-surface wind speeds were generally

https://doi.org/10.5194/egusphere-2026-6551
Preprint. Discussion started: 6 November 2026
© Author(s) 2026. CC BY 4.0 License.

low (< 2 m s^{-1}), but exceeded 4 m s^{-1} during some periods. Air temperature showed clear diurnal variations with an overall increasing trend. Relative humidity followed a similar diurnal pattern, mostly ranging from 20 % to 60 % and reaching 50 %–70 % around 10–14 January. The stability parameter z/L exhibited both positive and negative variations, indicating the occurrence of unstable, near-neutral, and stable stratification during the pollution episodes.

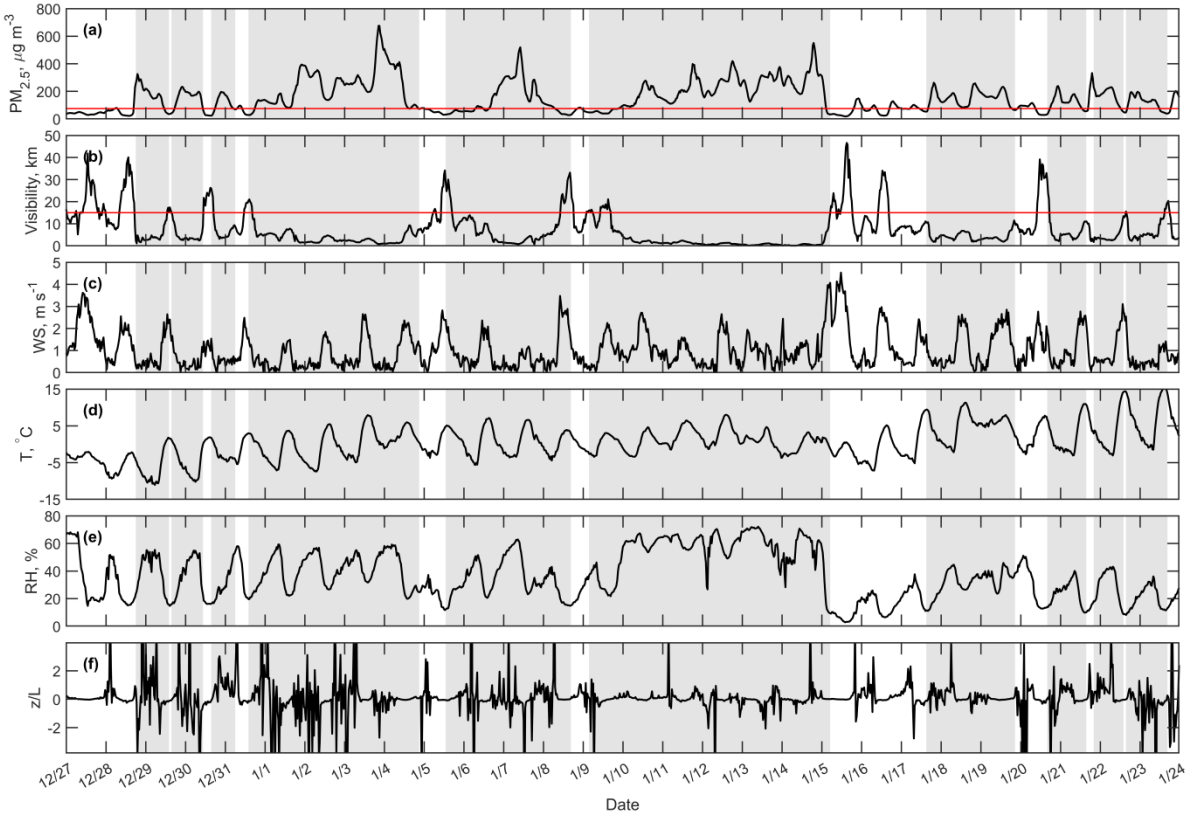


Figure 2: Time series of $PM_{2.5}$ (a), visibility (b), wind speed (c), air temperature (d), relative humidity (e), and stability parameter (f) from 27 December 2018 to 24 January 2019.

3.2 Episode-specific visibility-$PM_{2.5}$ conversion and its influence on turbulent flux estimation

The optimal visibility–$PM_{2.5}$ conversion forms varied among different pollution episodes. Representative cases with the best fits obtained by the exponential, quadratic polynomial, reciprocal, and power-law models are shown in Fig 3a-d, respectively. All models reproduced the rapid decrease in $PM_{2.5}$ concentration with increasing visibility and the gradual flattening at higher visibility levels. The representative cases all achieved R^2 values above 0.90. The optimal function forms and fitted parameters differed substantially among pollution episodes. This indicates that the visibility–$PM_{2.5}$ relationship is process- dependent and cannot be adequately described by a single fixed function for all episodes. Figure 3e-f further compares the fitting performance of the different models across all pollution episodes. The quadratic, exponential, and power-law models generally yielded high R^2 and low RMSE values. In contrast, the reciprocal model performed well in some pollution episodes but showed a much

https://doi.org/10.5194/egusphere-2026-6551
Preprint. Discussion started: 6 November 2026
© Author(s) 2026. CC BY 4.0 License.

wider RMSE range, indicating stronger episode dependence. In summary, the best-fit model selected for each pollution episode gave more consistent R^2 and RMSE values, indicating that episode-specific model selection improves the fitting performance of the visibility–$PM_{2.5}$ relationship.

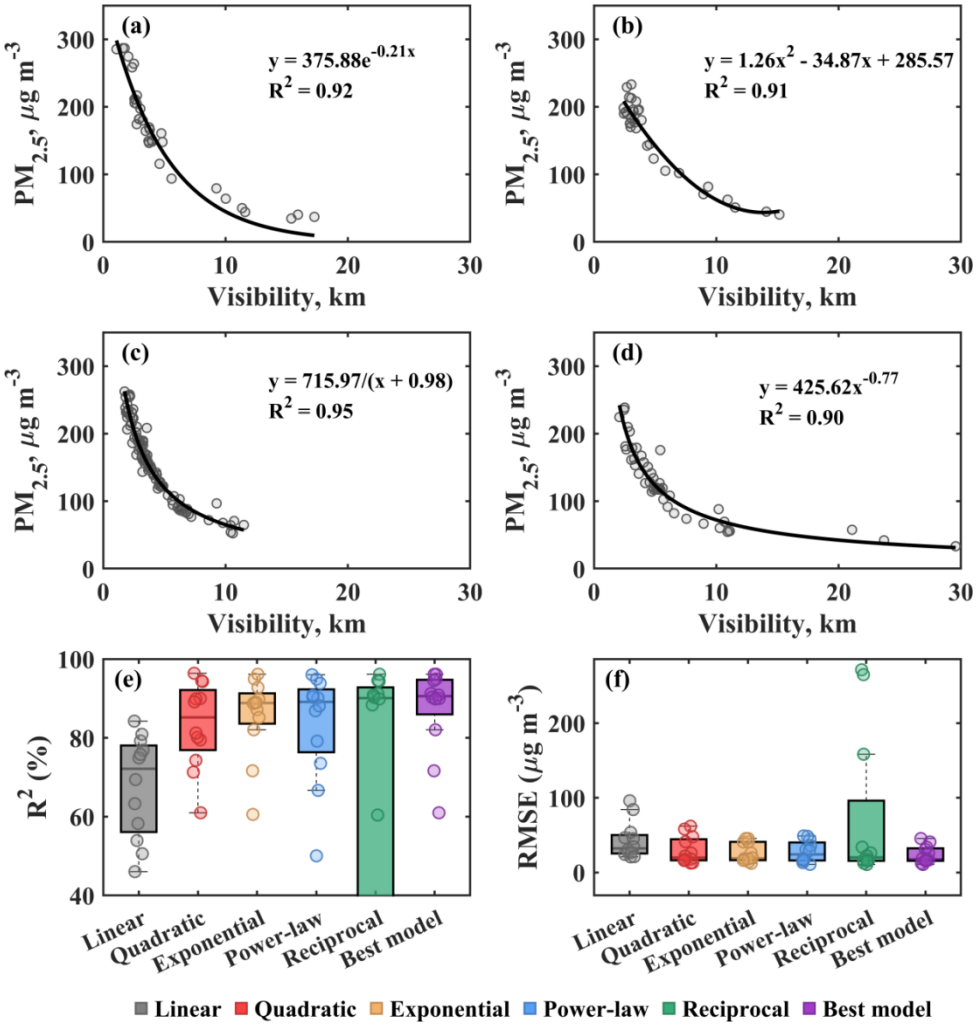


Figure 3: Fitting results of the visibility–$PM_{2.5}$ relationship and comparison of model performance. (a–d) Representative fits of the exponential, quadratic, reciprocal, and power-law models, respectively. (e, f) Distributions of R^2 and RMSE for the candidate models and the best-fit model selected for each pollution episode.

The best-fit model selected for each pollution episode was applied to the corresponding 1 Hz visibility series to retrieve high-frequency $PM_{2.5}$ mass concentrations. After mean detrending, the resulting fluctuations were used to calculate the turbulent flux using the eddy covariance method: $F_{PM_{2.5}} = \overline{w'c'}$. The episode-specific best-fit approach was further compared with the fixed power-law method of Ren et al. (2020). In Fig. 4, the former is labeled "new" and the latter "old".

https://doi.org/10.5194/egusphere-2026-6551
Preprint. Discussion started: 6 November 2026
© Author(s) 2026. CC BY 4.0 License.

The two methods produced broadly consistent $PM_{2.5}$ fluctuation standard deviations and turbulent fluxes, with different sensitivities to model selection. Most standard deviations from the episode-specific and fixed power-law approaches clustered near the 1:1 line, indicating similar $PM_{2.5}$ variability. For high-variability cases, however, the fixed power-law approach yielded larger values, suggesting greater sensitivity to the conversion relationship (Fig. 4a). Flux estimates from both approaches were also generally close to the 1:1 relationship. Greater scatter at low flux magnitudes indicates a clear influence of the conversion relationship on flux estimation (Fig. 4b).

To remove dimensional dependence and quantify differences symmetrically, we defined the symmetric relative differences in fluctuation standard deviation and turbulent flux as follows:

$$\Delta\sigma_{c,sym} = \frac{\sigma_{c,new} - \sigma_{c,old}}{0.5\left(\sigma_{c,new} + \sigma_{c,old}\right)}$$

$$\Delta F_{sym} = \frac{F_{new} - F_{old}}{0.5\left(\left|F_{new}\right| + \left|F_{old}\right|\right)}$$

The distributions of the symmetric relative differences with visibility (Fig. 4c–d) showed substantially greater scatter in $\Delta\sigma_{c,sym}$ and ΔF_{sym} under low-visibility conditions, with both positive and negative deviations. Both metrics gradually converged toward zero as visibility increased. Samples from different stability regimes largely overlapped across visibility ranges, without clear grouping. Thus, the differences between the two approaches were concentrated under low-visibility conditions, corresponding to severe pollution episodes. Accordingly, selecting an appropriate empirical visibility–$PM_{2.5}$ relationship for each pollution episode is important for accurately estimating fine-particle mass fluxes. The fluctuations and fluxes retrieved using this approach were subsequently used to compare the turbulent transport characteristics of $PM_{2.5}$ and conventional scalars.

https://doi.org/10.5194/egusphere-2026-6551
Preprint. Discussion started: 6 November 2026
© Author(s) 2026. CC BY 4.0 License.

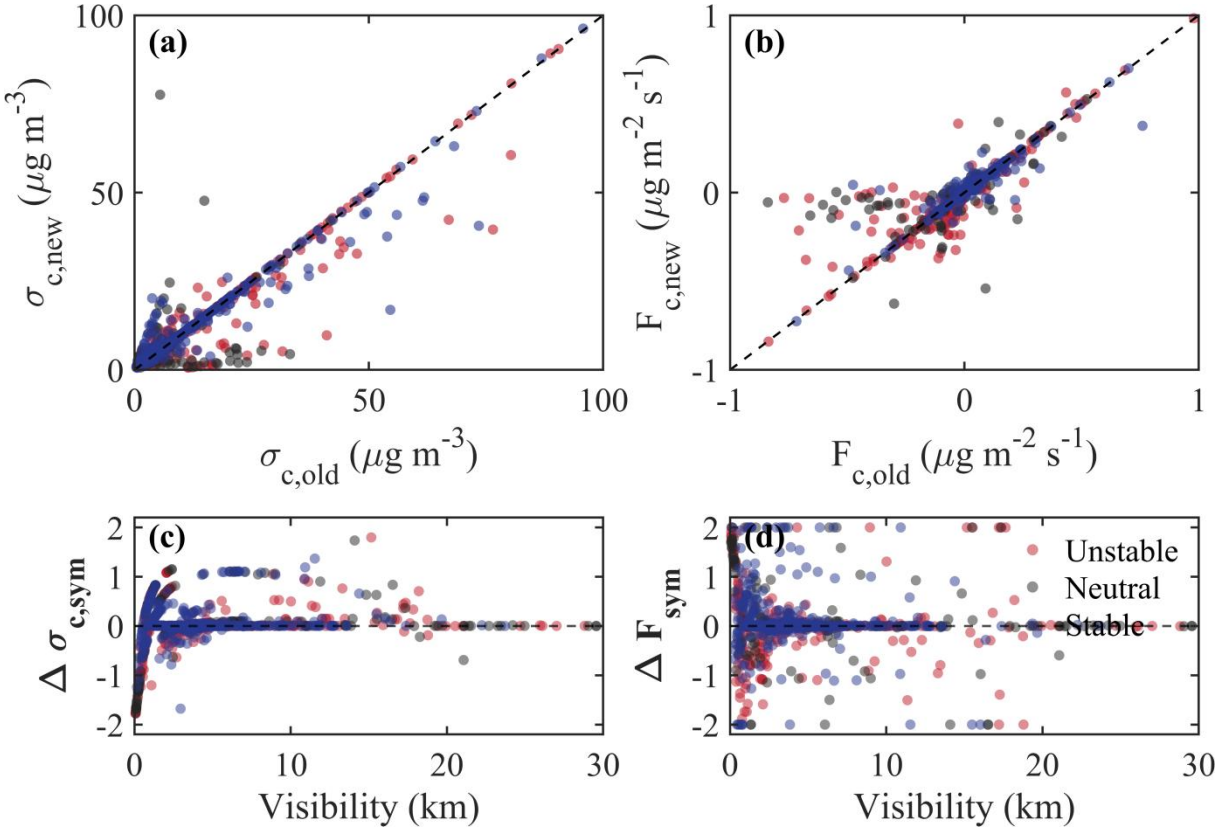


Figure 4: Comparison of $PM_{2.5}$ concentration fluctuation standard deviations and turbulent fluxes obtained using the episode-specific best-fit approach (new) and the fixed power-law method (old). (a) $\sigma_{c,new}$ versus $\sigma_{c,old}$ (b) F_{new} versus F_{old} (c, d) Corresponding symmetric relative differences, $\Delta\sigma_{c,sym}$ and ΔF_{sym}, as functions of visibility.

3.3 Variance scaling and vertical transport efficiency of $PM_{2.5}$

Using the $PM_{2.5}$ concentration fluctuations and fluxes derived from the episode-specific visibility–$PM_{2.5}$ relationships, we compared the turbulent transport characteristics of $PM_{2.5}$ with those of conventional meteorological scalars. Figure 5 shows the variation of normalized standard deviations of $PM_{2.5}$, CO_2, water vapour q, and temperature T with the stability parameter ζ. Under unstable stratification, the normalized standard deviations of all four scalars decreased with increasing $-\zeta$ and followed an approximate $(-\zeta)^{-1/3}$ relationship. Samples under stable stratification were more dispersed and did not show an equally clear scaling.

The fitted coefficients were 3.68 for $PM_{2.5}$, 2.65 for CO_2, 1.67 for water vapour, and 1.13 for temperature. The fitted coefficients for water vapour and temperature were comparable to previous near-surface observations (Gao et al., 2006), suggesting that the normalized standard deviations of these two scalars showed reasonable magnitudes and followed the expected stability dependence. The normalized standard deviation of CO_2 was generally higher than those of water vapour and temperature, consistent with reported differences among scalar flux–variance relationships (Zahn et al., 2023; Mack et al.,

https://doi.org/10.5194/egusphere-2026-6551
Preprint. Discussion started: 6 November 2026
© Author(s) 2026. CC BY 4.0 License.

2024). Compared with conventional scalars, $PM_{2.5}$ showed a larger fitted coefficient, indicating a greater concentration variability relative to its flux scale under the same unstable conditions. The distributional comparison in Appendix A supports this result: $PM_{2.5}$ had a broader, more right-skewed distribution than water vapour and temperature, and its distribution was closest to that of CO_2 (Fig. A1; Table A1).

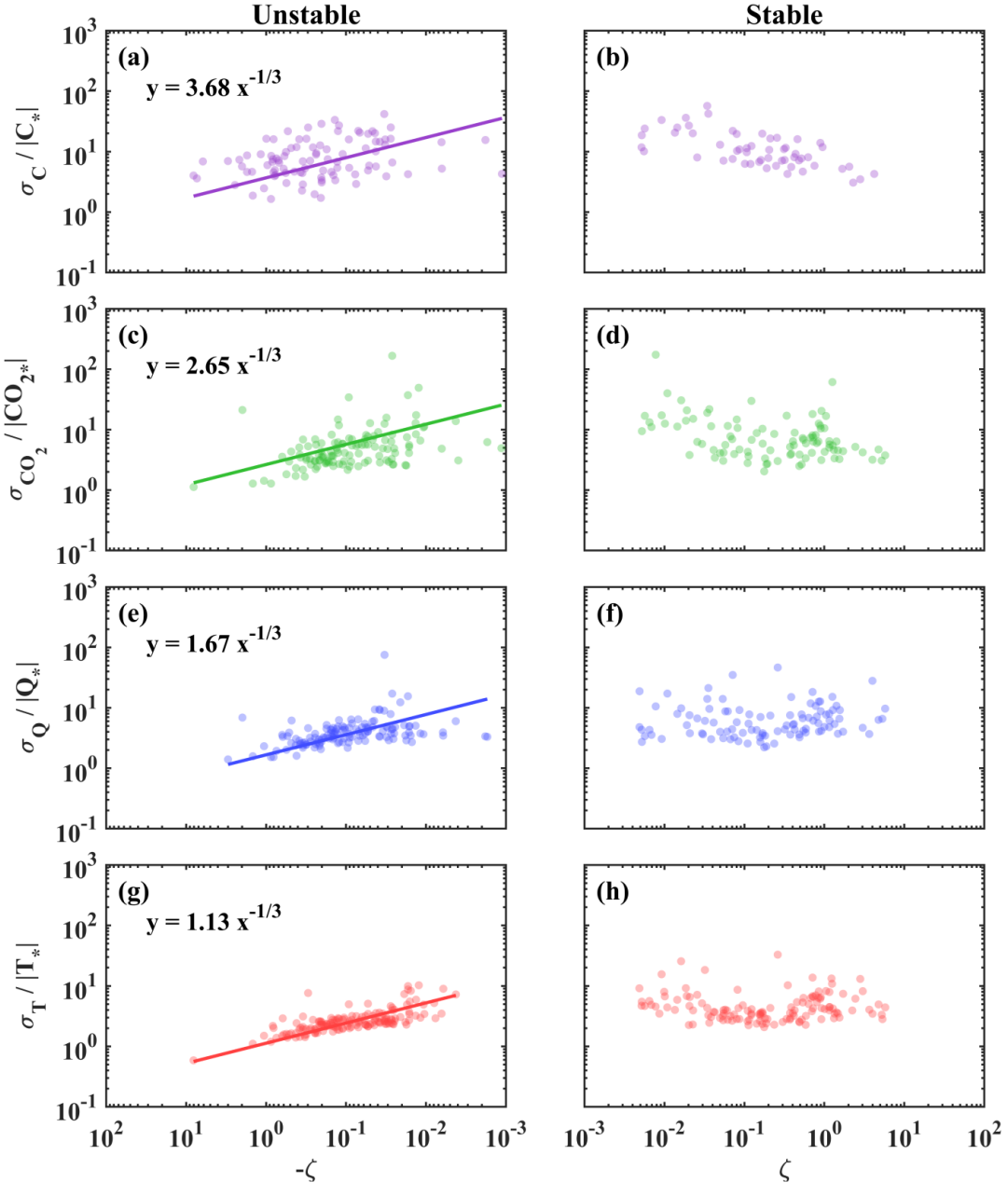


Figure 5: Normalized standard deviation of $PM_{2.5}$, CO_2, water vapour q, and temperature T as a function of stability parameter ζ under unstable and stable stratification.

https://doi.org/10.5194/egusphere-2026-6551
Preprint. Discussion started: 6 November 2026
© Author(s) 2026. CC BY 4.0 License.

The normalized standard deviation is directly related to the correlation coefficient between vertical velocity and scalar fluctuations. For any scalar s, the flux scale is defined as $s_* = \left|\overline{w's'}\right| / u_*$; then

$$\frac{\sigma_s}{|s_*|} = \frac{u_*}{\sigma_s}\frac{1}{|r_{ws}|}, r_{ws} = \frac{\overline{w's'}}{\sigma_w \sigma_s}$$

Therefore, within the same observation period, a larger normalized standard deviation corresponds to a smaller absolute correlation coefficient. The larger scaling coefficient of $PM_{2.5}$ indicates that its concentration fluctuations are greater relative to the net flux, corresponding to a lower normalized transport efficiency. To further investigate this feature and its stability dependence, Fig. 6 compares the correlations between vertical velocity and the fluctuations of $PM_{2.5}$, CO_2, water vapour, and temperature across stability conditions. The sign of the correlation coefficient represents the direction of turbulent transport, whereas its absolute value reflects the coupling strength between vertical velocity and scalar fluctuations. The absolute correlation coefficient was therefore used to quantify the normalized vertical transport efficiency. Figure 6a–h presents the overall variations in correlation coefficients with stability parameter. We divided $|\zeta|$ into 11 logarithmically spaced bins from 10^{-3} to 10^{1} and calculated the median and interquartile range in each bin. The threshold of $|\zeta| = 0.05$ was used to distinguish unstable, near neutral, and stable conditions. To facilitate the description of correlation changes under different stability regimes, $|\zeta| = 0.05$ was further introduced as an auxiliary reference boundary. Conditions with $|\zeta| > 0.5$ and $0.05 < |\zeta| < 0.5$ were classified as strong and weak unstable or stable regimes, respectively.

The correlations between conventional scalars and vertical velocity showed clear stability responses that varied among scalars (Fig. 6c–h). Under unstable conditions, CO_2 generally showed negative correlations, whereas water vapour and temperature were mainly positively correlated with vertical velocity. Compared with stronger instability ($\zeta < -0.05$), the three scalars generally exhibited stronger correlations under weaker instability ($-0.5 < \zeta < -0.05$), with the correlation strength decreasing as conditions approached neutrality. In stable conditions, CO_2 maintained a weak positive correlation with vertical velocity and showed little variation with stability, whereas the positive correlation of water vapour and the negative correlation of temperature generally weakened as stability increased. These results indicate that conventional scalars exhibit clear responses to atmospheric stratification, while the correlation direction and sensitivity to stability vary among scalars.

Compared with conventional scalars, $PM_{2.5}$ showed much weaker correlations with vertical velocity, with a less distinct dependence on stability (Fig. 6a,b). The median absolute correlation coefficients of $PM_{2.5}$ were 0.072 under unstable conditions and 0.059 under stable conditions. These values were substantially lower than those of CO_2, water vapour, and temperature, which ranged from 0.272 to 0.461 under unstable conditions and from 0.164 to 0.246 under stable conditions. The median correlation coefficients of $PM_{2.5}$ remained small across most stability ranges, although the maximum absolute values reached 0.666 under unstable conditions and 0.614 under stable conditions. Positive and negative $PM_{2.5}$ correlations accounted for 31.1 % and 68.9 % of the samples under unstable conditions, and 62.4 % and 37.6 % under stable conditions. Thus, both transport direction and coupling strength varied substantially among $PM_{2.5}$ samples.

https://doi.org/10.5194/egusphere-2026-6551
Preprint. Discussion started: 6 November 2026
© Author(s) 2026. CC BY 4.0 License.

To further quantify the differences in vertical transport efficiency between $PM_{2.5}$ and conventional scalars, we defined $\Delta R = |r_{w,s}| - |r_{w,c}|$, where s represent CO_2, water vapour, and temperature, respectively, and c represents $PM_{2.5}$. In most stability bins, the median ΔR was positive (Fig. 6i), indicating weaker coupling between $PM_{2.5}$ and vertical velocity than between the conventional scalars and vertical velocity. The difference was largest for temperature, followed by water vapour, and smallest for CO_2. It was most pronounced under unstable conditions and generally decreased towards near-neutral and stable states. Among the conventional scalars, CO_2 had the most similar transport efficiency to $PM_{2.5}$.

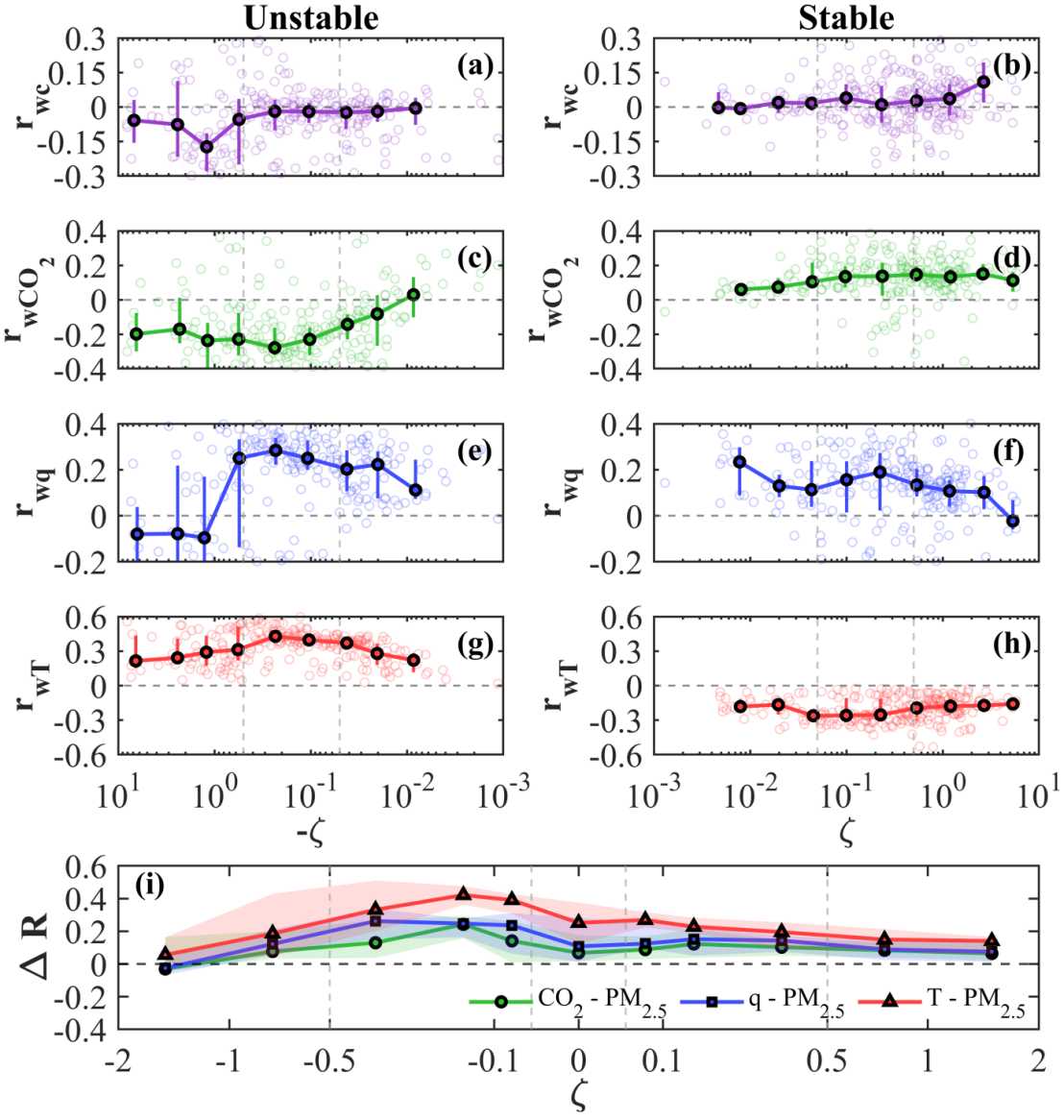


Figure 6: Correlations between vertical velocity and $PM_{2.5}$, CO_2, water vapour q, and temperature T under unstable and stable stratification, and differences among the scalars. Filled circles show median correlations within each stability bin; vertical bars show the 25th–75th percentile range.

https://doi.org/10.5194/egusphere-2026-6551
Preprint. Discussion started: 6 November 2026
© Author(s) 2026. CC BY 4.0 License.

3.4 Quadrant organization of instantaneous turbulent-flux events

To further explain the event structures associated with the weak correlation between $PM_{2.5}$ and vertical velocity in Fig. 6, quadrant analysis and hole analysis were applied to compare the flux contributions from the four quadrants under different hole thresholds H. As the hole threshold increased, weaker instantaneous flux events were gradually excluded, leaving only events with larger flux magnitudes. Figure 7 uses the maximum single quadrant contribution $Q_{\max}$ and normalized quadrant entropy H_Q to characterize the concentration and dispersion of flux contributions among the four quadrants, respectively.

With increasing H, $Q_{\max}$ rose and H_Q fell for all four scalars, indicating that the retained strong instantaneous flux events became increasingly concentrated in fewer quadrants (Fig. 7). CO_2, water vapour, and temperature showed clear increases in $Q_{\max}$, with temperature exhibiting the strongest quadrant concentration. In contrast, $PM_{2.5}$ consistently had the lowest $Q_{\max}$ and the highest H_Q under both unstable and stable conditions, with only small changes as H increased. Thus, even among strong events, conventional scalar flux contributions were more concentrated in a few quadrants, whereas $PM_{2.5}$ contributions remained more dispersed.

This result provides an event-level interpretation of the weaker $PM_{2.5}$ correlations shown in Fig. 6. $PM_{2.5}$ was not lacking in strong instantaneous flux events; however, the flux contributions remained dispersed among the four quadrants, with both events aligned with and opposite to the net flux making notable contributions. This dispersed contribution pattern is consistent with the weaker correlation between $PM_{2.5}$ and vertical velocity. The detailed hole-size dependence of event fractions and absolute flux contributions is shown in Appendix B (Figs. B1 and B2).

https://doi.org/10.5194/egusphere-2026-6551
Preprint. Discussion started: 6 November 2026
© Author(s) 2026. CC BY 4.0 License.

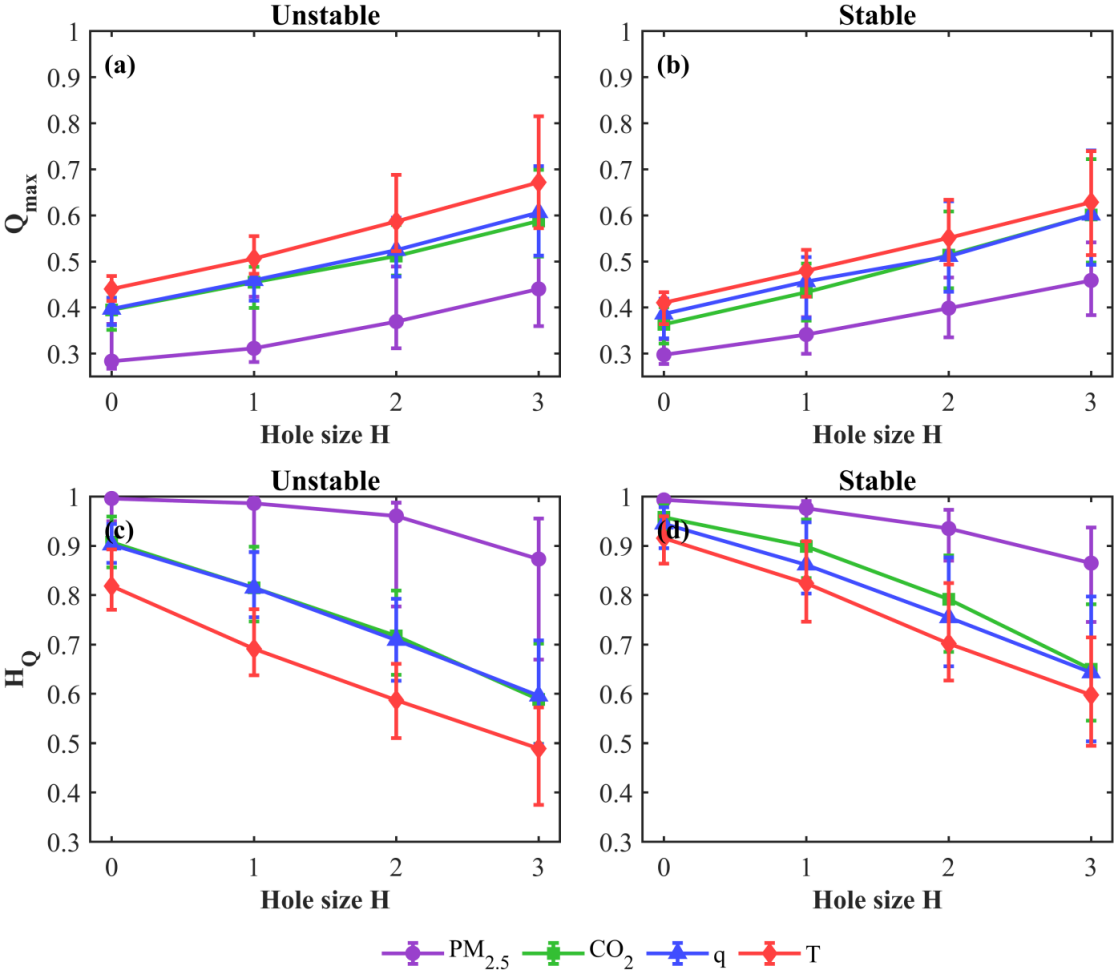


Figure 7: Maximum quadrant contribution, Q_{max}, and normalized quadrant entropy, H_Q, as a function of hole size H for different scalars under unstable and stable conditions.

3.5 Scale-dependent characteristics of $PM_{2.5}$ turbulent fluxes

To identify the contribution of different frequencies to transport differences, Fig. 8 compares the normalized variance spectra, cospectra, squared coherence spectra, and phase spectra of the four scalars. All four scalars exhibited high premultiplied normalized variance spectra within the range of approximately 0.005–0.02 Hz, corresponding to timescales of about 50–200 s. $PM_{2.5}$ had a smaller relative variance contribution at higher frequencies than the conventional scalars. This difference was clearest for negative $PM_{2.5}$ flux under unstable conditions and positive flux under stable conditions.

The cospectra and coherence spectra further suggest that only a small fraction of $PM_{2.5}$ concentration fluctuations can effectively contribute to flux through coupling with vertical velocity. Under unstable conditions with positive $PM_{2.5}$ flux, temperature squared coherence was approximately 0.25–0.40 between 0.01 and 0.08 Hz; water vapour and CO_2 were lower, while $PM_{2.5}$ squared coherence was mostly below 0.10. This indicates weak linear coupling between $PM_{2.5}$ fluctuations and

https://doi.org/10.5194/egusphere-2026-6551
Preprint. Discussion started: 6 November 2026
© Author(s) 2026. CC BY 4.0 License.

vertical velocity over that frequency range. Under stable conditions, coherence decreased overall for all scalars, while $PM_{2.5}$ remained at a relatively low level.

After aligning the phase according to the net flux direction of each scalar, the phases of CO_2, water vapour, and temperature were mostly close to zero within the 0.01–0.10 Hz range, suggesting relatively stable synchronization with vertical velocity. In contrast, the phase of $PM_{2.5}$ varied substantially, with some frequencies approaching $\pm\pi/2$ or $\pm\pi$. Together with the low coherence of $PM_{2.5}$, the large phase dispersion suggests that phase relationships become less stable when the coupling with vertical velocity is weak.

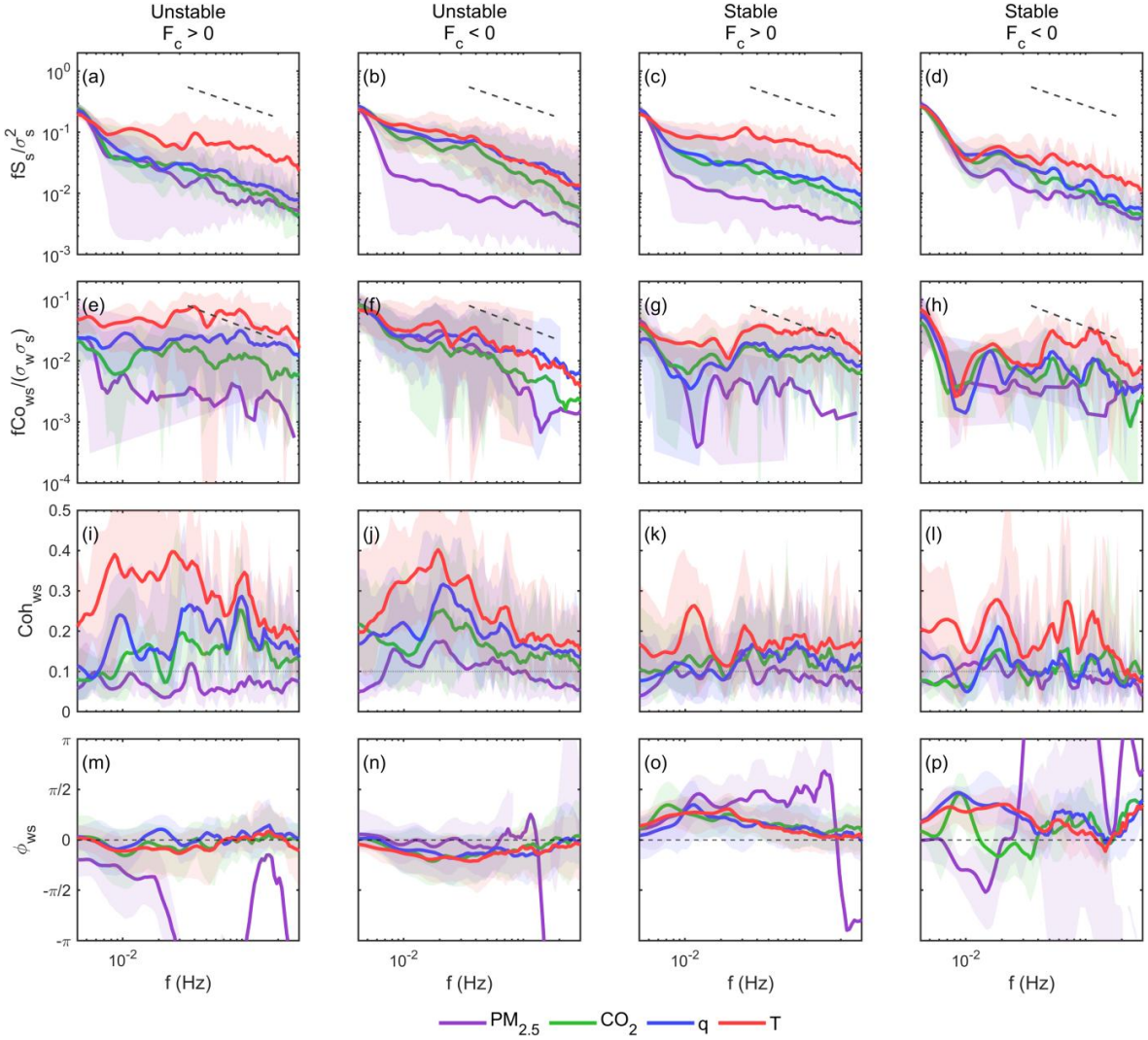


Figure 8: Spectral characteristics of $PM_{2.5}$, CO_2, water vapour q, and temperature T for different stability conditions and $PM_{2.5}$ flux directions. (a–d) Frequency-premultiplied normalized variance spectra; (e–h) frequency-premultiplied normalized cospectra of vertical velocity and each scalar; (i–l) squared coherence; (m–p) phase. Columns show unstable conditions with positive and negative $PM_{2.5}$ flux, followed by stable conditions with positive and negative $PM_{2.5}$ flux.

https://doi.org/10.5194/egusphere-2026-6551
Preprint. Discussion started: 6 November 2026
© Author(s) 2026. CC BY 4.0 License.

To further examine whether flux contributions at different frequency scales accumulate in the same direction or cancel each other during integration, Fig. 9a–d presents the normalized signed Ogive curves of $PM_{2.5}$, CO_2, water vapour, and temperature under different stability conditions and $PM_{2.5}$ flux directions. The cumulative amplitudes of all scalars remained small at frequencies above 0.1 Hz, suggesting a limited contribution of this high frequency range to the total flux. As frequency decreased further, the Ogive curves changed mainly within the range of approximately 10^{-3}–10^{-1} Hz, showing that the net flux was mainly determined by cospectral contributions across different frequency scales in this range.

The Ogive curves of water vapour and temperature were relatively smooth under all four conditions and generally varied monotonically. The Ogive curve for water vapour remained positive and generally increased as the integration extended toward lower frequencies, indicating that the cumulative contribution was dominated by positive transport. For temperature, the curve was positive under unstable conditions and negative under stable conditions, corresponding to upward and downward sensible heat transport. At the lowest frequencies, both curves approached their maximum normalized amplitudes. This suggests little cancellation from low frequency contributions and broadly consistent flux directions across scales. For CO_2, the cumulative contribution was mainly negative in unstable conditions and became positive in stable conditions. Although CO_2 showed greater scatter than water vapour and temperature, its Ogive curve remained relatively continuous and monotonic. This pattern suggests that the dominant frequency contributions to CO_2 flux also had a fairly consistent sign.

$PM_{2.5}$ exhibited a distinctly different accumulation pattern from the conventional scalars. For unstable conditions with ($Fc > 0$), the $PM_{2.5}$ Ogive curve reached only about 0.5 at the lowest frequencies rather than approaching the normalized upper limit of 1. Several local fluctuations were also evident within the 10^{-2}–10^{-1} Hz range. This pattern suggests that contributions at intermediate frequencies initially produced a relatively large positive cumulative flux. As lower frequency contributions were added, however, the cumulative value decreased, indicating cospectral contributions at low frequencies with a sign opposite to the net flux.

A similar cancellation across frequency scales also occurred under stable conditions with $Fc < 0$. In this case, the $PM_{2.5}$ Ogive curve displayed a clear change in slope and pronounced fluctuations near 10^{-2} Hz. Its absolute magnitude at the lowest frequencies also remained well below 1, suggesting positive cospectral contributions at some frequencies that opposed the overall negative flux. For unstable negative flux and stable positive flux conditions, the $PM_{2.5}$ Ogive curves were relatively more continuous, but their cumulative amplitudes at the lowest frequencies remained below those of the conventional scalars. As lower frequency contributions were progressively included, cospectral contributions of the opposite sign still reduced the cumulative flux established at higher frequencies. The relatively wide interquartile ranges further indicate substantial differences among samples in both flux accumulation processes and the degree of cancellation across frequency scales.

Based on the above Ogive characteristics, the net cospectral consistency index R_{net} was used to quantitatively assess the sign consistency of cospectral contributions across different frequency scales (Fig. 9e–h). Across the four conditions, water vapour and temperature showed generally high values of R_{net}, with most samples approaching 1. This suggests that contributions from different frequency scales were largely consistent in sign for their net fluxes. Although R_{net} of CO_2 showed some

https://doi.org/10.5194/egusphere-2026-6551
Preprint. Discussion started: 6 November 2026
© Author(s) 2026. CC BY 4.0 License.

variability, it remained substantially higher than that of $PM_{2.5}$ overall. The $PM_{2.5}$ median ranged from 0.126 to 0.381 and its distribution was broader. The difference was largest under unstable conditions with positive flux: the median was 0.126 for $PM_{2.5}$, compared with 0.962 for CO_2, 0.956 for q, and 0.988 for T. These values show that $PM_{2.5}$ flux included more contributions with opposing signs and stronger cancellation across scales. These results reveal that $PM_{2.5}$ flux contributions across different frequency scales have weaker sign consistency. Cospectral contributions with opposite signs can reduce the cumulative flux that has already been established by contributions at other frequencies. Therefore, the formation of $PM_{2.5}$ net fluxes is strongly affected by cancellation across frequency scales. Together with the quadrant results, the spectral analysis shows that $PM_{2.5}$ flux contributions are less directionally organized among events and less consistent in sign across frequencies. Both features help explain its lower normalized transport efficiency. Thus, scalars can share a similar variance-scaling exponent while differing substantially in how their transport contributions accumulate to form net flux.

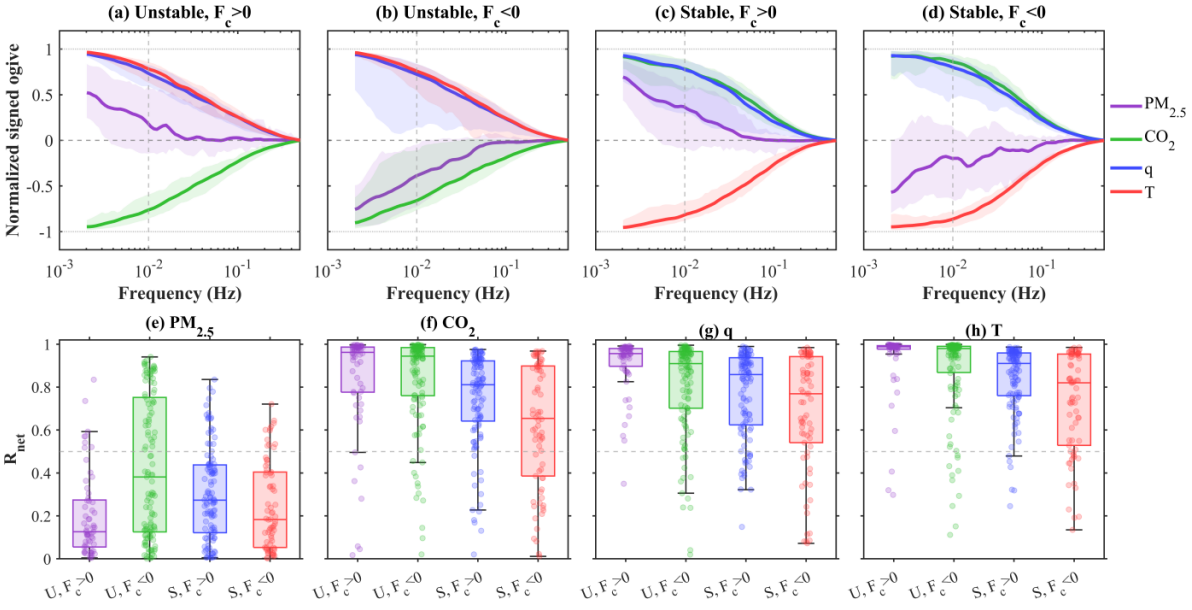


Figure 9: Normalized signed Ogive curves and net cospectral consistency (R_{net}) for $PM_{2.5}$, CO_2, water vapour q, and temperature T under different stability conditions and $PM_{2.5}$ flux directions. (a–d) Normalized signed Ogive curves under unstable conditions with positive and negative $PM_{2.5}$ flux and stable conditions with positive and negative $PM_{2.5}$ flux, respectively. Lines and shading show the median and interquartile range; the vertical dashed line marks f = 0.01 Hz. (e–h) R_{net} for $PM_{2.5}$, CO_2, q, and T under the same four regimes; each point represents a 30 min sample, with colour denoting $PM_{2.5}$ turbulent flux.

4 Conclusions

Using wintertime near-surface observations in Dezhou, North China Plain, this study developed an episode-specific method for retrieving $PM_{2.5}$ mass concentration fluctuations from visibility measurements. This study compared $PM_{2.5}$ with CO_2, water vapour, and temperature in terms of variance scaling, correlations with vertical velocity, and event and frequency contributions to turbulent fluxes. The main conclusions are as follows.

https://doi.org/10.5194/egusphere-2026-6551
Preprint. Discussion started: 6 November 2026
© Author(s) 2026. CC BY 4.0 License.

(1) An episode-specific approach was developed to select visibility–$PM_{2.5}$ empirical relationships, improving the estimation of $PM_{2.5}$ concentration fluctuations and turbulent fluxes compared with the use of a single fixed relationship. The visibility $PM_{2.5}$ relationship varied among pollution episodes. After selecting the optimal empirical relationship for each pollution episode, the fitted R^2 and RMSE values became more stable across episodes, reducing the fitting biases associated with applying one fixed relationship to different pollution conditions. The turbulent mass fluxes derived from the episode-specific models were generally consistent with those from the fixed power-law method. However, differences in both concentration fluctuations and flux estimates increased under low-visibility conditions, suggesting greater sensitivity to the conversion relationship during heavy pollution periods. These results suggest that selecting visibility–$PM_{2.5}$ relationships according to individual pollution episodes can better represent different pollution conditions and improve the assessment of $PM_{2.5}$ fluctuations and turbulent fluxes.

(2) This study found that similar variance-scaling exponents coexist with markedly different normalized vertical transport efficiencies. Under unstable stratification, the normalized standard deviations of $PM_{2.5}$, CO_2, water vapour, and temperature approximately followed a $(-\zeta)^{-1/3}$ scaling relationship, with fitted coefficients of 3.68, 2.65, 1.67, and 1.13, respectively. $PM_{2.5}$ exhibited a similar stability response, but the larger coefficient for $PM_{2.5}$ indicates stronger concentration fluctuations relative to its flux scale. However, this similarity in variance scaling did not extend to vertical transport. Under both unstable and stable conditions, $PM_{2.5}$ was less correlated with vertical velocity than the conventional scalars. Its transport direction and coupling strength also varied considerably among samples. Thus, similar variance-scaling exponents do not imply comparable net transport efficiency. Among the conventional scalars, CO_2 had the smallest difference in vertical-velocity coupling from $PM_{2.5}$, particularly under unstable conditions.

(3) The event and frequency contribution characteristics that explain the lower transport efficiency of $PM_{2.5}$ were identified. Even when only strong instantaneous flux events were retained, $PM_{2.5}$ flux contributions remained more widely distributed among the quadrants than those of conventional scalars, with both upward and downward contributions present. In the frequency domain, $PM_{2.5}$ exhibited weaker coherence with vertical velocity, together with stronger cancellation between positive and negative cospectral contributions. Across the four combinations of stability conditions and $PM_{2.5}$ flux directions, the median net cospectral consistency index of $PM_{2.5}$ ranged only from 0.126 to 0.381, remaining lower than those of the conventional scalars. The dispersed directionality of event contributions and the cancellation among different frequency contributions jointly explain the weaker overall coupling between $PM_{2.5}$ and vertical velocity. These findings highlight the importance of directional consistency among transport contributions in determining net transport efficiency.

This study links variance scaling and transport efficiency to the formation of net turbulent fluxes. Although $PM_{2.5}$ and conventional scalars exhibit similar variance-scaling exponents under unstable conditions, their transport contributions differ in directional consistency and cancellation across frequencies. These findings provide observational insight into near-surface pollutant exchange and vertical redistribution during winter. The episode-specific retrieval method supports the estimation of $PM_{2.5}$ concentration fluctuations and turbulent fluxes. The transport findings provide a basis for assessing the applicability of

https://doi.org/10.5194/egusphere-2026-6551
Preprint. Discussion started: 6 November 2026
© Author(s) 2026. CC BY 4.0 License.

shared turbulent diffusion relationships in air quality models and developing parameterizations that account for differences between particulate matter and conventional scalars.

Appendix A

The probability-density distributions of normalized standard deviation for all four scalars were unimodal, right-skewed, and had long tails (Fig. A1). Most samples had relatively small normalized fluctuations, while a few had larger values. Compared with water vapour and temperature, $PM_{2.5}$ had a broader distribution and a more pronounced high-value tail, indicating greater variability among observation periods. The CO_2 distribution was more similar to that of $PM_{2.5}$; the water-vapour and temperature distributions were more concentrated, with the largest difference from $PM_{2.5}$ for temperature.

The distribution metrics in Table A1 confirm that $PM_{2.5}$ was most similar to CO_2: the KS distance was 0.2606, the JS divergence was 0.0411, and the PDF overlap was 0.8029. Similarity was next highest for water vapour, while temperature differed most. Together with the stability scaling in Fig. 5, these results indicate similarities in both stability response and overall distribution shape. The larger $PM_{2.5}$ scaling coefficient and broader distribution may also reflect the combined influence of spatially heterogeneous emissions, deposition, and particle microphysical processes. CO_2 showed the closest distributional similarity to $PM_{2.5}$ among the tested conventional scalars.

https://doi.org/10.5194/egusphere-2026-6551
Preprint. Discussion started: 6 November 2026
© Author(s) 2026. CC BY 4.0 License.

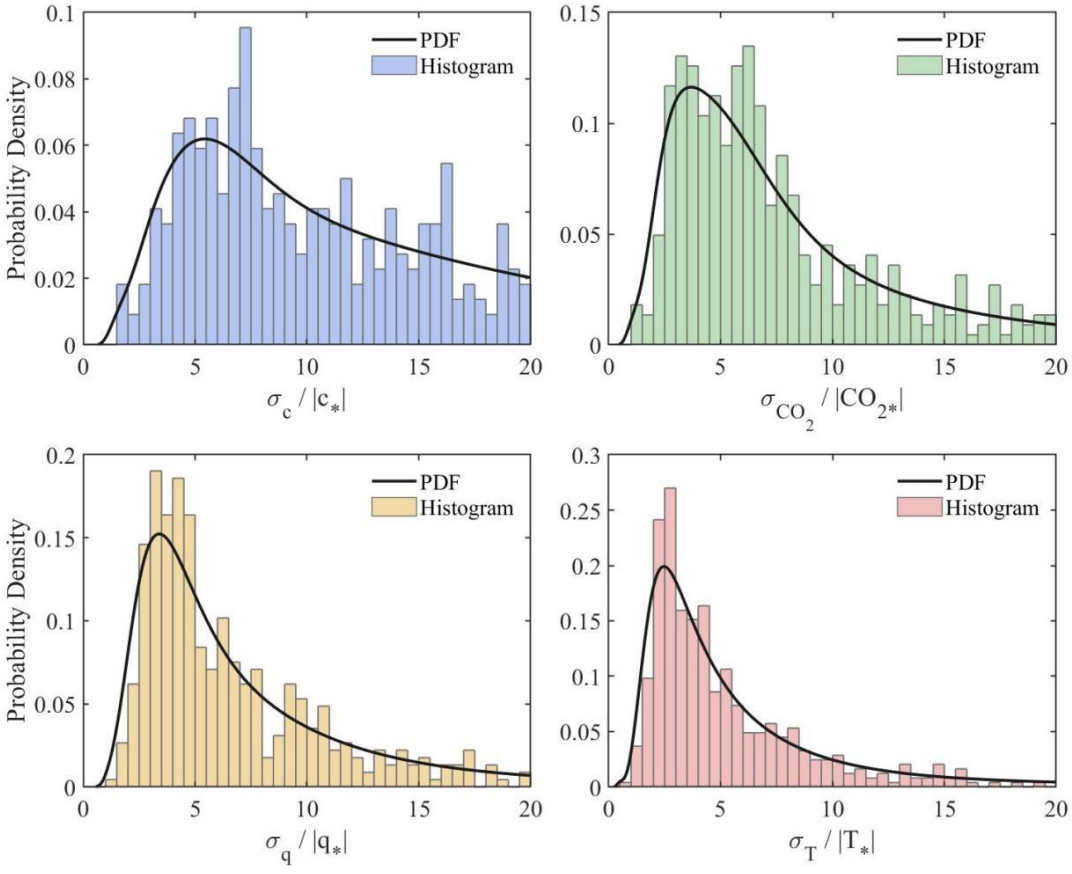


Figure A1: Probability-density distributions of normalized standard deviations for $PM_{2.5}$, CO_2, water vapour q, and temperature T. Histograms show the sample distributions; solid curves show the fitted probability density functions.

Table A1: Similarity metrics for the distributions of normalized standard deviations of $PM_{2.5}$ and conventional scalars.

Scalar	KS Distance	JS Divergence	PDF Overlap
CO_2	0.2606	0.0411	0.8029
q	0.3320	0.0714	0.7318
T	0.4744	0.1699	0.5935

Appendix B

Figures B1 and B2 compare event fractions and absolute flux contributions among the four quadrants as the hole-size threshold H increases. The stronger separation among quadrants for the conventional scalars indicates that their strong fluxes become concentrated in particular coherent motions.

https://doi.org/10.5194/egusphere-2026-6551
Preprint. Discussion started: 6 November 2026
© Author(s) 2026. CC BY 4.0 License.

CO_2, water vapour, and temperature showed clear quadrant selectivity. As H increased, event fractions and flux contributions in Q2 and Q4 decreased, while Q1 and Q3 became dominant. Under unstable conditions, strong CO_2 and water-vapour transport was shared by Q1 and Q3, so both upward and downward motions aligned with the net flux. Temperature contributions increasingly concentrated in Q1, consistent with strong sensible-heat transport by upward motions aligned with the net flux. Under stable conditions, all three conventional scalars increasingly concentrated in Q3, indicating that stronger transport was more often carried by downward motions aligned with the net flux. Thus, stronger events for conventional scalars became concentrated in fewer organized motions as H increased.

$PM_{2.5}$ showed less separation among quadrants as H increased. Under unstable conditions, contributions changed only gradually. Under stable conditions, Q3 increased, but Q1, Q2, and Q4 remained appreciable. Even at H = 3, strong $PM_{2.5}$ fluxes were shared among several quadrants rather than concentrated in a stable dominant structure. Event fractions and absolute flux contributions followed broadly similar patterns. For conventional scalars, Q1 or Q3 generally combined a high event fraction with a large flux contribution; $PM_{2.5}$ contributions were more evenly distributed. This indicates that strong $PM_{2.5}$ fluxes did not arise from a small number of consistently dominant coherent events.

https://doi.org/10.5194/egusphere-2026-6551
Preprint. Discussion started: 6 November 2026
© Author(s) 2026. CC BY 4.0 License.

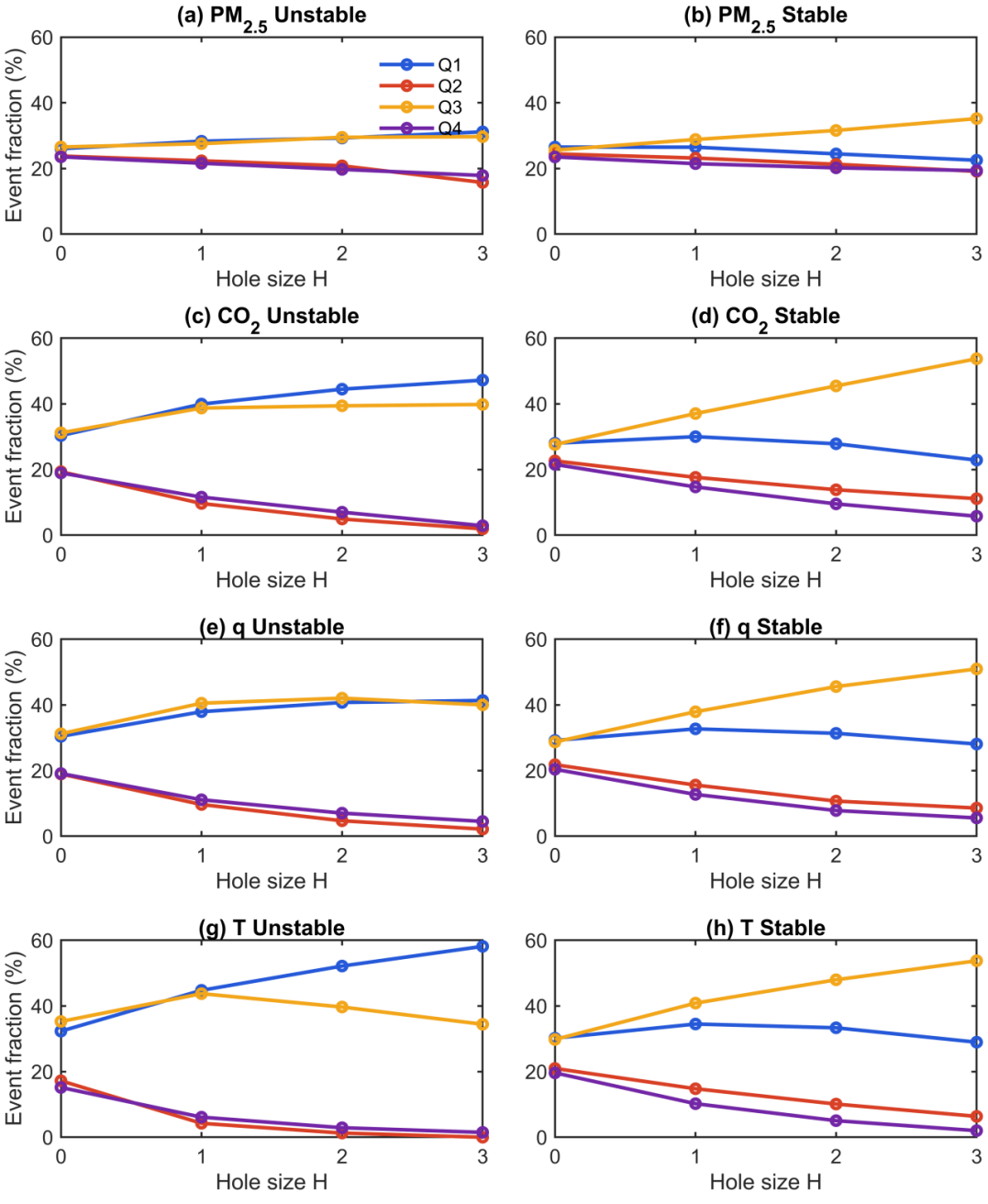


Figure B1: Fractions of events in each quadrant for $PM_{2.5}$, CO_2, water vapour q, and temperature T as a function of hole size H under unstable and stable conditions.

https://doi.org/10.5194/egusphere-2026-6551
Preprint. Discussion started: 6 November 2026
© Author(s) 2026. CC BY 4.0 License.

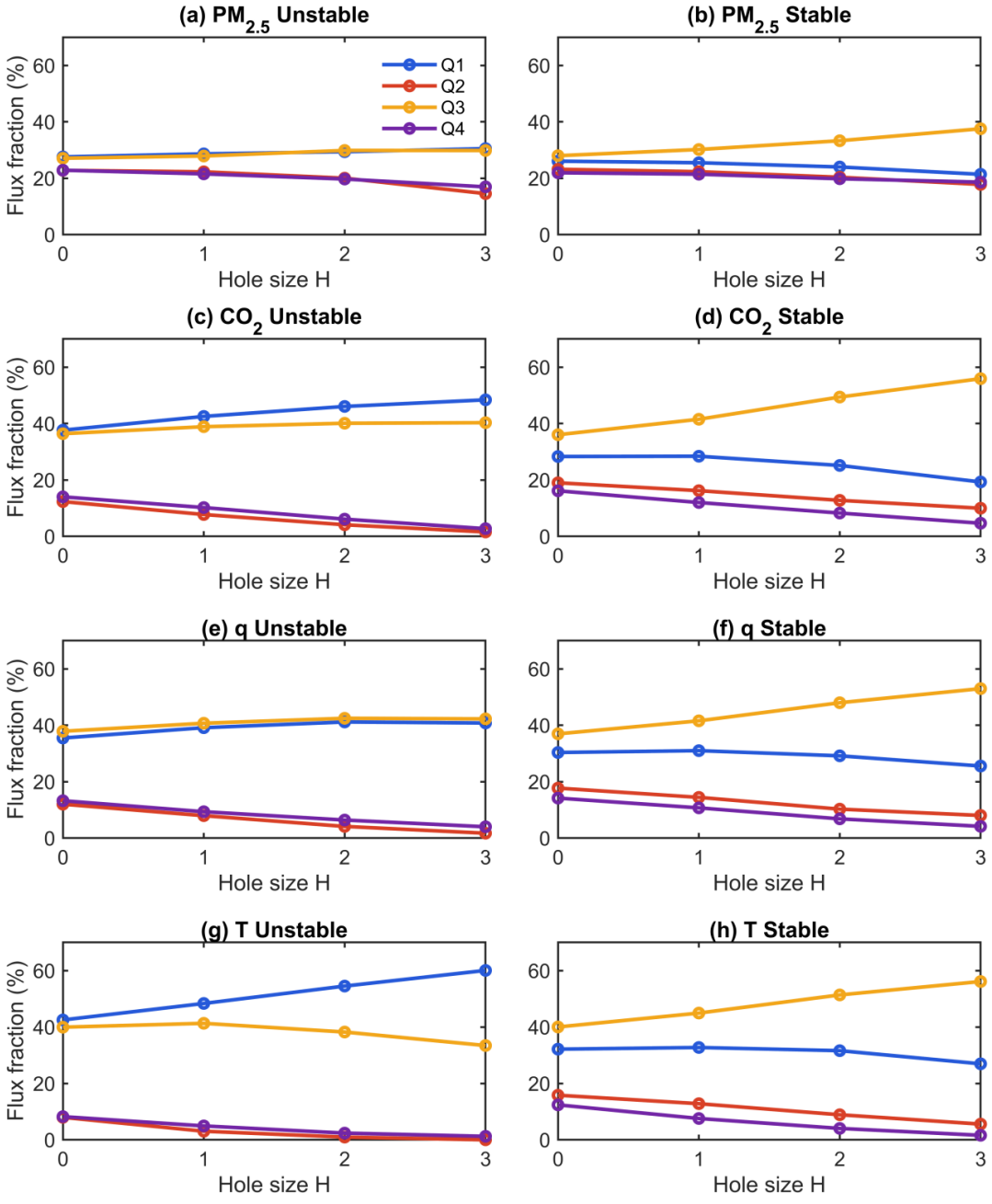


Figure B2: Absolute flux-contribution fractions in each quadrant for $PM_{2.5}$, CO_2, water vapour q, and temperature T as a function of hole size H under unstable and stable conditions.

Data availability

The data used in this study are available from the corresponding author upon request.

https://doi.org/10.5194/egusphere-2026-6551
Preprint. Discussion started: 6 November 2026
© Author(s) 2026. CC BY 4.0 License.

Author contribution

WJ: data curation, formal analysis, methodology, software, writing–original draft, writing–review and editing. YR: conceptualization, formal analysis, funding acquisition, methodology, supervision, project administration, resources, writing–original draft, writing–review and editing. HZ: conceptualization, funding acquisition, project administration, resources, writing–original draft, writing–review and editing. JL: investigation, resources, writing–review and editing. XC: investigation, resources, writing–review and editing. PT: data curation. LZ: investigation, resources, writing–review and editing. JH: investigation, resources, writing–review and editing.

Competing interests

At least one of the (co-)authors is a member of the editorial board of Atmospheric Chemistry and Physics.

Financial support

This work was supported by the Jing-Jin-Ji Regional Integrated Environmental Improvement–National Science and Technology Major Project (Project No. 2026ZD1210300), the National Natural Science Foundation of China (Grant Nos. 42475184, 42305071), and the Fundamental Research Funds for the Central Universities (lzujbky-2026-jdzx07 and lzujbky-2026-ey01).

References

Baldocchi, D. D.: How eddy covariance flux measurements have contributed to our understanding of Global Change Biology, Global Change Biol., 26, 242–260, https://doi.org/10.1111/gcb.14807, 2020.

Baldocchi, D., Falge, E., Gu, L., Olson, R., Hollinger, D., Running, S., Anthoni, P., Bernhofer, C., Davis, K., Evans, R., Fuentes, J., Goldstein, A., Katul, G., Law, B., Lee, X., Malhi, Y., Meyers, T., Munger, W., Oechel, W., Paw U, K. T., Pilegaard, K., Schmid, H. P., Valentini, R., Verma, S., Vesala, T., Wilson, K., and Wofsy, S.: FLUXNET: A new tool to study the temporal and spatial variability of ecosystem-scale carbon dioxide, water vapor, and energy flux densities, B. Am. Meteorol. Soc., 82, 2415–2434, https://doi.org/10.1175/1520-0477(2001)082<2415:FANTTS>2.3.CO;2, 2001.

Burnett, R., Chen, H., Szyszkowicz, M., Fann, N., Hubbell, B., Pope, C. A., Apte, J. S., Brauer, M., Cohen, A., Weichenthal, S., Coggins, J., Di, Q., Brunekreef, B., Frostad, J., Lim, S. S., Kan, H., Walker, K. D., Thurston, G. D., Hayes, R. B., Lim, C. C., Turner, M. C., Jerrett, M., Krewski, D., Gapstur, S. M., Diver, W. R., Ostro, B., Goldberg, D., Crouse, D. L., Martin, R. V., Peters, P., Pinault, L., Tjepkema, M., van Donkelaar, A., Villeneuve, P. J., Miller, A. B., Yin, P., Zhou, M., Wang, L., Janssen, N. A. H., Marra, M., Atkinson, R. W., Tsang, H., Thach, T. Q., Cannon, J. B., Allen, R. T., Hart, J. E., Laden, F., Cesaroni, G., Forastiere, F., Weinmayr, G., Jaensch, A., Nagel, G., Concin, H., and Spadaro, J. V.: Global estimates of

https://doi.org/10.5194/egusphere-2026-6551
Preprint. Discussion started: 6 November 2026
© Author(s) 2026. CC BY 4.0 License.

mortality associated with long-term exposure to outdoor fine particulate matter, P. Natl. Acad. Sci. USA, 115, 9592–9597, https://doi.org/10.1073/pnas.1803222115, 2018.

Cheng, Z., Ma, X., He, Y., Jiang, J., Wang, X., Wang, Y., Sheng, L., Hu, J., and Yan, N.: Mass extinction efficiency and extinction hygroscopicity of ambient $PM_{2.5}$ in urban China, Environ. Res., 156, 239–246, https://doi.org/10.1016/j.envres.2017.03.022, 2017.

de Jesus, A. L., Rahman, M. M., Mazaheri, M., Thompson, H., Knibbs, L. D., Jeong, C., Evans, G., Nie, W., Ding, A., Qiao, L., Li, L., Portin, H., Niemi, J. V., Timonen, H., Luoma, K., Petäjä, T., Kulmala, M., Kowalski, M., Peters, A., Cyrys, J., Ferrero, L., Manigrasso, M., Avino, P., Buonanno, G., Reche, C., Querol, X., Beddows, D. C. S., Harrison, R. M., Sowlat, M. H., Sioutas, C., and Morawska, L.: Ultrafine particles and $PM_{2.5}$ in the air of cities around the world: Are they representative of each other?, Environ. Int., 129, 118–135, https://doi.org/10.1016/j.envint.2019.05.021, 2019.

Dupont, S., Rajot, J.-L., Labiadh, M., Bergametti, G., Lamaud, E., Irvine, M. R., Alfaro, S. C., Bouet, C., Fernandes, R., Khalfallah, B., Marticorena, B., Bonnefond, J. M., Chevaillier, S., Garrigou, D., Henry-des-Tureaux, T., Sekrafi, S., and Zapf, P.: Dissimilarity between dust, heat, and momentum turbulent transports during aeolian soil erosion, J. Geophys. Res.-Atmos., 124, 1064–1089, https://doi.org/10.1029/2018JD029048, 2019.

Gao, Z., Bian, L., Chen, Z., Sparrow, M., and Zhang, J.: Turbulent variance characteristics of temperature and humidity over a non-uniform land surface for an agricultural ecosystem in China, Adv. Atmos. Sci., 23, 365–374, https://doi.org/10.1007/s00376-006-0365-y, 2006.

Guo, X., Zhang, H., Cai, X., Kang, L., Zhu, T., and Leclerc, M. Y.: Flux-variance method for latent heat and carbon dioxide fluxes in unstable conditions, Bound.-Lay. Meteorol., 131, 363–384, https://doi.org/10.1007/s10546-009-9377-3, 2009.

Hicks, B. B. and Baldocchi, D. D.: Measurement of fluxes over land: Capabilities, origins, and remaining challenges, Bound.-Lay. Meteorol., 177, 365–394, https://doi.org/10.1007/s10546-020-00531-y, 2020.

Jia, W. and Zhang, X.: Impact of modified turbulent diffusion of $PM_{2.5}$ aerosol in WRF-Chem simulations in eastern China, Atmos. Chem. Phys., 21, 16827–16841, https://doi.org/10.5194/acp-21-16827-2021, 2021.

Jia, W., Zhang, X., Zhang, H., and Ren, Y.: Application of turbulent diffusion term of aerosols in mesoscale model, Geophys. Res. Lett., 48, e2021GL093199, https://doi.org/10.1029/2021GL093199, 2021.

Jia, W., Zhang, X., Zhang, H., and Ren, Y.: Turbulent transport dissimilarities of particles, momentum, and heat, Environ. Res., 211, 113111, https://doi.org/10.1016/j.envres.2022.113111, 2022.

Jin, X., Cai, X., Yu, M., Song, Y., Wang, S., Kang, L., and Zhang, H.: Diagnostic analysis of wintertime $PM_{2.5}$ pollution in the North China Plain: The impacts of regional transport and atmospheric boundary layer variation, Atmos. Environ., 224, 117346, https://doi.org/10.1016/j.atmosenv.2020.117346, 2020.

Katul, G., Hsieh, C.-I., Kuhn, G., Ellsworth, D., and Nie, D.: Turbulent eddy motion at the forest-atmosphere interface, J. Geophys. Res.-Atmos., 102, 13409–13421, https://doi.org/10.1029/97JD00777, 1997.

Li, D. and Bou-Zeid, E.: Coherent structures and the dissimilarity of turbulent transport of momentum and scalars in the unstable atmospheric surface layer, Bound.-Lay. Meteorol., 140, 243–262, https://doi.org/10.1007/s10546-011-9613-5, 2011.

https://doi.org/10.5194/egusphere-2026-6551
Preprint. Discussion started: 6 November 2026
© Author(s) 2026. CC BY 4.0 License.

Li, Q., Wu, B., Liu, J., Zhang, H., Cai, X., and Song, Y.: Characteristics of the atmospheric boundary layer and its relation with $PM_{2.5}$ during haze episodes in winter in the North China Plain, Atmos. Environ., 223, 117265, https://doi.org/10.1016/j.atmosenv.2020.117265, 2020.

Li, Z., Guo, J., Ding, A., Liao, H., Liu, J., Sun, Y., Wang, T., Xue, H., Zhang, H., and Zhu, B.: Aerosol and boundary-layer interactions and impact on air quality, Natl. Sci. Rev., 4, 810–833, https://doi.org/10.1093/nsr/nwx117, 2017.

Lu, S. S. and Willmarth, W. W.: Measurements of the structure of the Reynolds stress in a turbulent boundary layer, J. Fluid Mech., 60, 481–511, https://doi.org/10.1017/S0022112073000315, 1973.

Luan, T., Guo, X., Guo, L., and Zhang, T.: Quantifying the relationship between $PM_{2.5}$ concentration, visibility and planetary boundary layer height for long-lasting haze and fog–haze mixed events in Beijing, Atmos. Chem. Phys., 18, 203–225, https://doi.org/10.5194/acp-18-203-2018, 2018.

Mack, L., Berntsen, T. K., Vercauteren, N., and Pirk, N.: Transfer efficiency and organization in turbulent transport over alpine tundra, Bound.-Lay. Meteorol., 190, 38, https://doi.org/10.1007/s10546-024-00879-5, 2024.

Mårtensson, E. M., Nilsson, E. D., Buzorius, G., and Johansson, C.: Eddy covariance measurements and parameterisation of traffic related particle emissions in an urban environment, Atmos. Chem. Phys., 6, 769–785, https://doi.org/10.5194/acp-6-769-2006, 2006.

Miao, Y., Liu, S., Guo, J., Huang, S., Yan, Y., and Lou, M.: Unraveling the relationships between boundary layer height and $PM_{2.5}$ pollution in China based on four-year radiosonde measurements, Environ. Pollut., 243, 1186–1195, https://doi.org/10.1016/j.envpol.2018.09.070, 2018.

Moriwaki, R. and Kanda, M.: Local and global similarity in turbulent transfer of heat, water vapour, and CO_2 in the dynamic convective sublayer over a suburban area, Bound.-Lay. Meteorol., 120, 163–179, https://doi.org/10.1007/s10546-005-9034-4, 2006.

Pryor, S. C., Barthelmie, R. J., Larsen, S. E., and Sørensen, L. L.: Ultrafine particle number fluxes over and in a deciduous forest, J. Geophys. Res.-Atmos., 122, 405–422, https://doi.org/10.1002/2016JD025854, 2017.

Ren, Y., Zhang, H., Wei, W., Cai, X., and Song, Y.: Determining the fluctuation of $PM_{2.5}$ mass concentration and its applicability to Monin–Obukhov similarity, Sci. Total Environ., 710, 136398, https://doi.org/10.1016/j.scitotenv.2019.136398, 2020.

Ren, Y., Zhang, H., Zhang, X., Li, Q., Cai, X., Song, Y., Kang, L., and Zhu, T.: Temporal and spatial characteristics of turbulent transfer and diffusion coefficient of $PM_{2.5}$, Sci. Total Environ., 782, 146804, https://doi.org/10.1016/j.scitotenv.2021.146804, 2021.

Ripamonti, G., Järvi, L., Mølgaard, B., Hussein, T., Nordbo, A., and Hämeri, K.: The effect of local sources on aerosol particle number size distribution, concentrations and fluxes in Helsinki, Finland, Tellus B, 65, 19786, https://doi.org/10.3402/tellusb.v65i0.19786, 2013.

https://doi.org/10.5194/egusphere-2026-6551
Preprint. Discussion started: 6 November 2026
© Author(s) 2026. CC BY 4.0 License.

Sun, X., Zhao, T., Liu, D., Gong, S., Xu, J., and Ma, X.: Quantifying the influences of $PM_{2.5}$ and relative humidity on change of atmospheric visibility over recent winters in an urban area of East China, Atmosphere, 11, 461, https://doi.org/10.3390/atmos11050461, 2020.

Vong, R. J., Vong, I. J., Vickers, D., and Covert, D. S.: Size-dependent aerosol deposition velocities during BEARPEX'07, Atmos. Chem. Phys., 10, 5749–5758, https://doi.org/10.5194/acp-10-5749-2010, 2010.

Wang, H., Peng, Y., Zhang, X., Liu, H., Zhang, M., Che, H., Cheng, Y., and Zheng, Y.: Contributions to the explosive growth of $PM_{2.5}$ mass due to aerosol–radiation feedback and decrease in turbulent diffusion during a red alert heavy haze in Beijing–Tianjin–Hebei, China, Atmos. Chem. Phys., 18, 17717–17733, https://doi.org/10.5194/acp-18-17717-2018, 2018.

Wang, J.-L., Zhang, Y.-H., Shao, M., Liu, X.-L., Zeng, L.-M., Cheng, C.-L., and Xu, X.-F.: Quantitative relationship between visibility and mass concentration of PM2.5 in Beijing, J. Environ. Sci., 18, 475–481, https://hero.epa.gov/reference/7751470/, 2006.

Wang, X., Zhang, R., and Yu, W.: The effects of $PM_{2.5}$ concentrations and relative humidity on atmospheric visibility in Beijing, J. Geophys. Res.-Atmos., 124, 2235–2259, https://doi.org/10.1029/2018JD029269, 2019.

Yuan, R., Luo, T., Sun, J., Liu, H., Fu, Y., and Wang, Z.: A new method for estimating aerosol mass flux in the urban surface layer using LAS technology, Atmos. Meas. Tech., 9, 1925–1937, https://doi.org/10.5194/amt-9-1925-2016, 2016.

Yuan, R., Zhang, H., Hua, J., Liu, H., Wu, P., Zhu, X., and Sun, J.: Comparison of the imaginary parts of the atmospheric refractive index structure parameter and aerosol flux based on different measurement methods, Atmos. Meas. Tech., 17, 2089–2102, https://doi.org/10.5194/amt-17-2089-2024, 2024.

Zahn, E., Bou-Zeid, E., and Dias, N. L.: Relaxed eddy accumulation outperforms Monin–Obukhov flux models under non-ideal conditions, Geophys. Res. Lett., 50, e2023GL103099, https://doi.org/10.1029/2023GL103099, 2023.